

Cite this: *Nanoscale*, 2018, **10**, 11403

Resonant silicon nanoparticles with controllable crystalline states and nonlinear optical responses†

Sergey Makarov,^a Lada Kolotova,^{b,c} Sergey Starikov,^{b,d} Urs Zywietz^e and Boris Chichkov^{f,g}

High-throughput laser printing of resonant silicon nanoparticles has emerged as a novel tool for the fabrication of deeply subwavelength objects with various functionalities. The applications of resonant silicon nanoparticles crucially depend on their crystalline state. However, the ways to control the crystalline structure during laser printing remain unstudied. Here we demonstrate, both experimentally and theoretically, how the crystalline structure of silicon nanoparticles fabricated by a laser printing technique can be varied from almost amorphous to a polycrystalline state. In particular, we propose a method of crystalline structure control *via* changing the distance between the irradiated silicon film and the receiving substrate. This study allows the most optimal conditions for second harmonic generation to be revealed. We believe that the proposed method opens the door to fully controllable laser printing of functional nanoparticles and nanostructures.

Received 12th March 2018,
Accepted 28th May 2018
DOI: 10.1039/c8nr02057d
rsc.li/nanoscale

1. Introduction

Laser transfer (or printing) of nano- and micro-particles is one of the most flexible approaches to deposit optically resonant structures at desirable positions on a substrate.^{1–3} Laser fabricated resonant silicon nanoparticles⁴ have been employed for a broad range of applications, namely, for directional^{5,6} and tunable⁷ light scattering, sensing,⁸ nonlinear light frequency conversion,⁹ optical heating with nanothermometry,¹⁰ and monitoring of thermally induced chemical reactions.¹¹ The optical properties underlying these bright effects are strongly dependent on the crystalline state of the silicon.¹² In particular, light scattering differs significantly between amorphous and crystalline Si nanoparticles.^{13,14} Partial crystallinity of silicon nanoparticles results in a strong enhancement of second harmonic generation (SHG).⁹ Almost fully crystalline Si

nanoparticles represent an excellent tool for Raman based sensing approaches.^{10,11,15}

Despite the fact that the laser printing method has been used for various materials and applications,¹⁶ an effective method for control of the nanoparticles' crystalline state is still missing. This fact makes it difficult to compare directly the experimental results for nanoparticles created in different works, possessing either amorphous,¹³ nanograin,⁹ or crystalline states.^{15,17}

In this paper, for the first time to our knowledge, we employ a modified high-throughput method of laser printing¹³ to control and optimize the fabrication process of nanoparticles with a strong second-order nonlinear response. We optimize the effect of the polycrystalline structure by choosing specific laser printing conditions supported by rigorous theoretical analysis of the crystallization kinetics. In particular, we vary the distance (*z*) between the donor and receiver substrates, as schematically shown in Fig. 1, to control the time-of-flight and cooling rate of the printed nanoparticles. Our findings may open up novel prospects for the design of nonlinear subwavelength light sources with exceptional characteristics, fully integrated into Si-based nanoscale photonic circuits.

^aDepartment of Nanophotonics and Metamaterials, ITMO University, St Petersburg 197101, Russia. E-mail: s.makarov@metalab.ifmo.ru

^bJoint Institute for High Temperatures, Russian Academy of Sciences, Moscow 125412, Russia

^cMoscow Institute of Physics and Technology, Moscow 117303, Russia

^dRuhr-Universität Bochum, ICAMS, Bochum 44801, Germany

^eNanotechnology Department, Laser Zentrum Hannover e.V., Hannover D-30419, Germany

^fFederal Scientific Research Centre Crystallography and Photonics of Russian Academy of Sciences, Moscow 142190, Russia

^gLeibniz University Hannover, Institute of Quantum Optics, Welfengarten str. 1, Hannover 30167, Germany

† Electronic supplementary information (ESI) available. See DOI: 10.1039/C8NR02057D

2. Experimental

2.1. Laser printing

For the laser printing process, we employed a commercial femtosecond laser system: the Tsunami Femtosecond

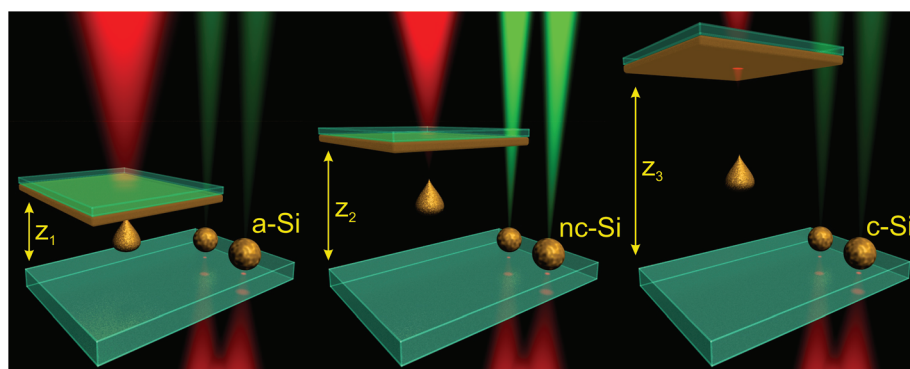


Fig. 1 The concept. Schematic illustration of laser printing at different distances between the donor (upper) and receiver (lower) substrates. In the central scenario, the nanoparticles are printed under the best conditions for second harmonic generation.

Oscillator and Spitfire Amplifier, Spectra Physics, generating laser pulses at an 800 nm central wavelength, with maximum pulse energies of up to 3 mJ, and a pulse duration of 50 fs at a repetition rate of 1 kHz. Laser pulses were tightly focused onto the front side of the Si films. A transparent (glass) receiver substrate was placed at a certain distance (z) on the other translation stage. For focusing, a microscope objective (Nikon) with $\times 50$ magnification and a numerical aperture (NA) of 0.45 was used. The Si nanoparticles were fabricated at laser energies $E < 10$ nJ.

As the source of the nanoparticles we used a 50 nm a -Si:H film (initial hydrogen concentration $\sim 10\%$), which was deposited on a substrate of fused silica by plasma enhanced chemical vapor deposition from SiH_3 precursor gas, as a sample for the nanoparticle fabrication. Samples were placed on a three-dimensional air-bearing translating stage driven by brushless servomotors (ABL1000, Aerotech), allowing a translation of samples with an accuracy better than 100 nm.

Generally, each laser pulse caused ejection of a single Si nanoparticle towards the receiver substrate. Fabricated nanoparticles were almost spherical,^{13,18} and their diameters were around 350 nm at the given laser pulse energy (for details, see ESI†). In order to visualize the arrays, the nanoparticles were illuminated by the s-polarized light from a halogen lamp (HL-2000-FHSA) at an angle of 65° to the surface normal, and a scattered signal was collected by means of an objective (Mitutoyo M Plan APO NIR $\times 50$, NA = 0.42).

As shown in Fig. 2, the best quality of laser printing was achieved at distances less than 8 μm . At the distance $z > 50$ μm , disordering of the particle array on the receiving substrate occurred (see Fig. 2). The disordering takes place as a result of initial fluctuation in the direction of nanoparticle motion. Our analysis showed that the fluctuation in the angle of nanoparticle motion is about 4° , as described in ESI.†

2.2. Raman measurements

In order to characterize the crystalline structure of the initial film and the printed individual nanoparticles, we acquired Raman scattering measurements. The Raman spectra were

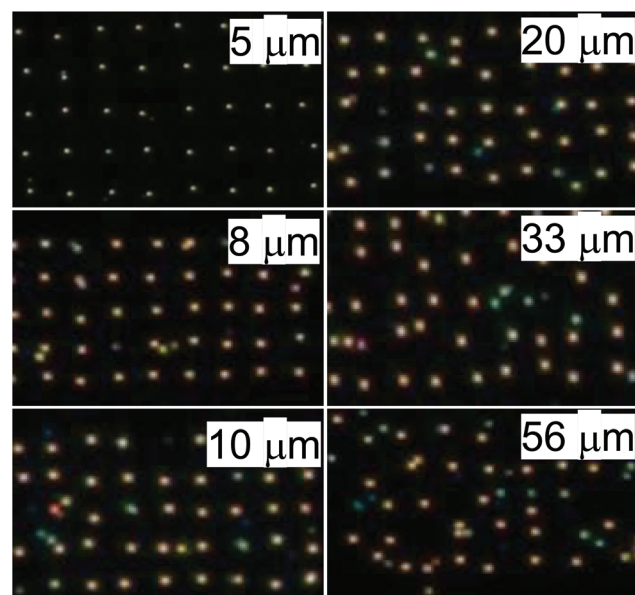


Fig. 2 The samples. Dark-field optical images at different distances between donor and receiver substrates: from 5 to 56 μm .

recorded by a micro-Raman apparatus (AIST-NTSmartSPM system with a Raman spectrometer HORIBA LabRam HR) under excitation by a 632.8 nm HeNe laser through a $\times 100$ microscope objective (NA = 0.9) and projected onto a thermoelectrically cooled charge-coupled device (Andor DU 420A-OE 325) with a 600 g mm^{-1} diffraction grating. The individual nanoparticles were placed by a piezo stage (AIST-NT) in the center of the focused laser beam (0.8 μm in diameter) with an accuracy of ~ 100 nm. Incident laser power was attenuated to avoid optical overheating of the studied Si nanoparticles.¹⁰

We characterized the initial a -Si:H film revealing its amorphous state from the observation of its broad Raman peak centered around 480 cm^{-1} .¹⁸ The reference Raman signal from a bulk crystalline silicon wafer and the literature data show that the Raman peak of the pure crystal with a cubic diamond structure corresponds to the optical phonon at 520 cm^{-1} .

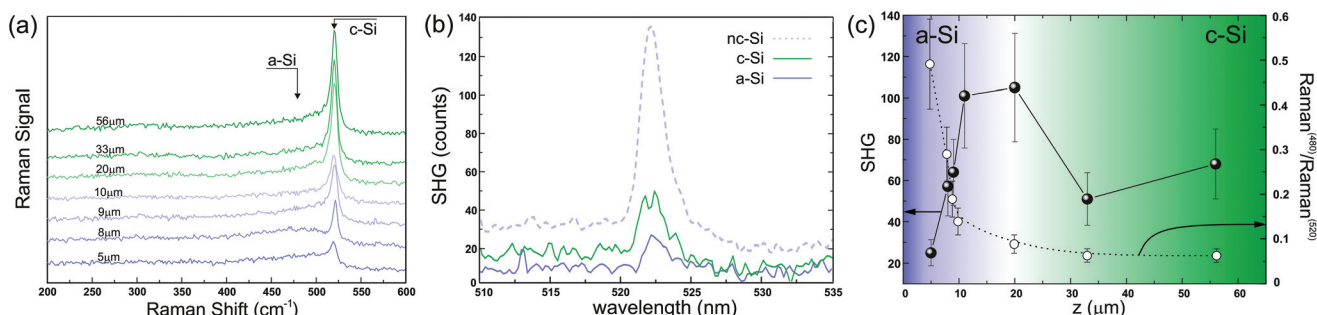


Fig. 3 Optical properties. (a) Raman spectra at different distances between donor and receiver substrates, written near each curve. (b) Signals of second harmonics generated from three silicon nanoparticles printed at different distances: 5 μm (purple solid curve), 10 μm (bright purple dashed curve), and 33 μm (green solid curve). (c) Dependences of the second harmonic signal (black dots) and the ratio of amorphous to crystalline Raman peaks (white dots) on the distance between donor and receiver substrates.

Since the spectral width of the crystalline peak is around 4.5 cm^{-1} , it is not overlapped too much with the amorphous peak, and the contributions from both phases can be clearly distinguished.¹⁹ In Fig. 3a, the dependence of the Raman signal on the distance between the surface of the silicon film and the receiving substrate is presented. Generally, the measured Raman spectra from individual nanoparticles possess narrow peaks at 520 cm^{-1} , standing on a wing of the broad amorphous peak at 480 cm^{-1} . The main tendency observed in our measurements is that the shorter the distance, the stronger the amorphous peak relative to the crystalline one. The ratio between the intensities of these peaks is plotted in Fig. 3c, where a gradual decrease of the amorphous fraction from 0.5 to 0.075 is shown. The maximum value corresponds to the distance between the substrates $z = 5 \mu\text{m}$ (see Fig. 3a). Apparently, such behavior is a result of different cooling conditions for various distances, which can be probed optically *via* second harmonic generation.⁹

2.3. Nonlinear optical measurements

According to our previous work,⁹ nanocrystalline silicon nanoparticles possess high second order nonlinear responses, owing to local symmetry breaking at the boundary interfaces. Here, we examined the correlation between the Raman spectra and second harmonic generation from the Si nanoparticles fabricated with various distances between the donor and receiver substrates.

A femtosecond Yb³⁺ laser (TeMa, Avesta Project) was used to generate a fundamental beam at 1050 nm (pulse duration 150 fs and repetition rate 80 MHz). After passing through an attenuator (a Glan prism coupled with a halfwave plate), the laser beam was focused onto the sample using a $\times 10/0.26$ NA microscope objective (Olympus). Samples were mounted on a 3 axis stage (Thorlabs) to precisely place the desired nanoparticle at the focus of the excitation laser with a maximum power of 200 μW . Laser energy was varied and controlled by a polarising filter and a power meter (Nova II, Ophir), respectively, while the pulse duration is measured by an autocorrelator ASF-20 (Avesta Project). The SH signal was collected by a

$\times 50/0.42$ NA objective (Mitutoyo M Plan APO NIR). The generated beam was filtered by a set of optical filters to remove the fundamental wavelength. The SH signal was focused onto the entrance slit of a Horiba LabRam HR spectrometer and projected onto a thermoelectrically cooled charge-coupled device (CCD, Andor DU 420A-OE 325) with a 150 g mm^{-1} diffraction grating. The time of signal collection was 10 seconds. An additional CCD camera (Canon 400 D) was used to take back-scattering linear and transmission nonlinear images. Statistical uncertainties in the SH signal measurements were determined by the values obtained after analysis of 15 nanoparticles (shown in Fig. 2) for each distance (z) between the substrates.

In Fig. 3b, we compare second harmonic signals from three silicon nanoparticles fabricated at different distances ($z = 5, 10$, and $33 \mu\text{m}$), when the laser intensity is fixed at $\sim 30 \text{ GW cm}^{-2}$. The strongest SH signal was emitted by the nanoparticle fabricated at $z = 10 \mu\text{m}$. A non-zero signal background in the SH spectra was caused by multiphoton luminescence from crystalline silicon (indirect semiconductor) observed in the entire visible range, when hot electrons decay radiatively *via* indirect transitions.²⁰ This is another probe for the crystalline state of silicon nanoparticles, because the purely amorphous state supports weak emission at lower frequencies ($\lambda > 500 \text{ nm}$ (ref. 21)).

As shown in Fig. 3c, the SH signal is the lowest for the closest distance z , where the amorphous component in Si nanoparticles dominates the crystalline one, according to the presented ratio between the amorphous and crystalline contributions to the Raman signals. With a further increase of z , one can observe a dramatic increase in SHG of up to 5 times and saturation around $z = 10\text{--}20 \mu\text{m}$, where the amorphous phase in the Raman spectra becomes weaker. At distances larger than $z = 20 \mu\text{m}$ SHG drops again and saturates at the values 2 times lower approximately, where the crystalline phase dominates in the Raman spectra.

Generally, the second-order polarization in centrosymmetric materials can be written as a superposition of the surface dipolar and bulk quadrupolar contributions.^{22–27}

However, for nanocrystalline silicon (ns-Si) particles the strongest contribution comes from the interfaces between the nanograins, described by the following term:⁹

$$\mathbf{P}_{\text{nc}}^{(2\omega)} \sim \mathbf{E}^{(\omega)} \nabla \cdot \mathbf{E}^{(\omega)}, \quad (1)$$

which gives zero SH yield from the homogeneous material of each silicon grain ($\nabla \cdot \mathbf{E}^{(\omega)} = 0$), whereas at the interfaces sharp changes of the lattice orientation play the role of SH sources. Thus, the more grains the higher the SH yield. While the amorphous state also can be considered as local inversion symmetry breaking due to defects in each unit cell, in reality such random material is optically homogeneous, and, therefore, has the vanishing term \mathbf{P}_{nc} .

In order to better understand under which conditions the phases of Si nanoparticles are the most appropriate for SHG, we discuss the cooling process in more detail.

3. Discussion

3.1. Initial stage

It can be assumed that the mechanism of nanoparticle formation in this work is similar to the laser ablation mechanism.^{28,29} When the absorbed laser energy becomes higher than a particular threshold value, a liquid droplet of molten material is detached from the film surface.^{13,30–32} The formation of the droplet goes through the following steps.^{29–32} After the laser pulse absorption, the film is radially heated, and melting takes place.^{33,34} Strong temperature increases and subsequent relaxation processes lead to the formation of a bubble. Two physical phenomena probably are the reason for these processes: mechanical stresses in the film due to shock wave propagation^{28,29} and evaporation at the interface between the film and glass substrate.^{30,35} Then, the bubble expands and accelerates the liquid shell in the direction perpendicular to the free substrate. Finally, due to the surface tension, the molten volume contracts to a sphere being ejected towards the receiver substrate. Such complex processes may be simulated by classical atomistic simulation.^{28,29}

The physical properties of formed nanoparticles can be estimated from experimental,^{30–32,35,36} theoretical^{31,32,35} and simulation^{29,37} analyses. The liquid droplet diameter was determined from SEM images. It depends on the laser fluence and the average values are equal to 100–500 nm.^{13,18,30,31} The initial velocity of the nanoparticles can be extracted from the time-resolved images of the liquid droplets. It strongly depends on the laser fluence, but in the nanoparticle formation regime the average value is approximately 100 m s⁻¹.^{31,35,37} The initial temperature of a nanoparticle can be calculated using theoretical or molecular dynamics two-temperature modeling.^{28,29,35,36} Based on these studies, the lattice temperature can be estimated as 2000 K (ref. 35) after the droplet detaching from the film surface.

3.2. Threshold cooling rate from atomistic simulations

For cooling of the formed liquid droplet with an initial temperature of 2000 K, the final structure strongly depends on the cooling rate K . Like in our previous work,³⁸ we performed the atomistic simulations of nanoparticle cooling with various values of K . The interactions between atoms were described by the angular-dependent interatomic potential developed on the basis of *ab initio* calculations.³⁸ The simulated system contained 171 360 Si atoms that formed a single nanowire with a diameter of about 36 nm. The simulations were carried out in the quasi-2D case: one of the sizes in the calculation cell was about 3.5 nm, and periodic boundary conditions were used. With the use of the Langevin thermostat the liquid nanowire was cooled down to room temperature. In this way, we estimated the threshold cooling rate for silicon crystallization: $K_{\text{th}} \approx 0.8 \text{ K ps}^{-1}$. At $K > K_{\text{th}}$, the atomic structure remained in the disordered state after the cooling process. As we show further, this cooling rate is close to the case of nanoparticle cooling on a glass surface, resulting in partial amorphisation. In turn, for $K < K_{\text{th}}$, silicon crystallization takes place. Fig. 4 shows the results of our atomistic simulations for various values of K . It should be noted that the smaller the K value, the larger the average size of the formed crystallines. For $K = 0.25 \text{ K ps}^{-1}$, the average size of the formed grains was about 8 nm, which correlated with previously reported values.⁹ It also worth nothing that in experiments on the dewetting of thin films in an oven to fabricate arrays of Si nanoparticles,^{39,40} the cooling rate that prevents their formation in the amorphous state is much lower.

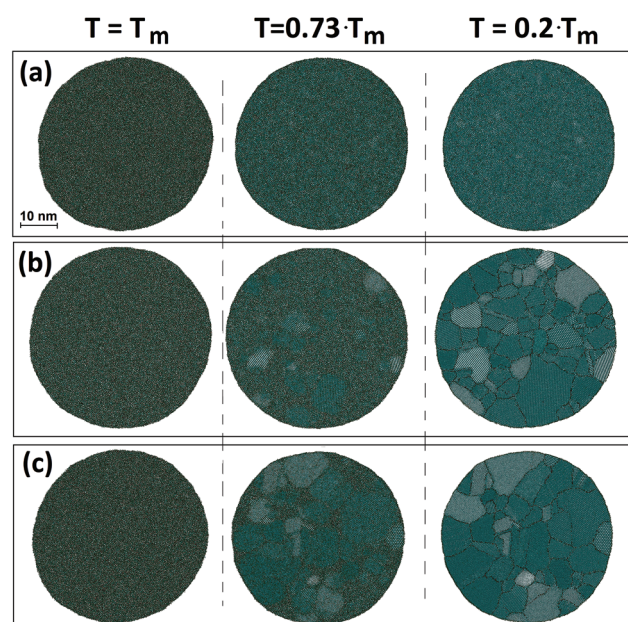


Fig. 4 Atomistic simulations. The evolution of atomic structures in the atomistic simulations with various cooling rates (the simulated systems in vertical rows have identical temperatures to that shown at the top of the figure): (a) $K = 2 \text{ K ps}^{-1}$; (b) $K = 0.6 \text{ K ps}^{-1}$; (c) $K = 0.25 \text{ K ps}^{-1}$.

In order to connect the atomistic simulations with the experimental data available, we estimated the cooling rate K for laser printing under different conditions. There are two regimes for the cooling: movement in air from the irradiated film to the receiver substrate; and cooling by direct contact with the receiving substrate.

3.3. Cooling in air

During the movement from the irradiated film to the receiving substrate, nanoparticles are cooled by collisions with air molecules. K may be estimated with use of the Fourier expression for heat flux q :

$$q = \chi \frac{T - T_{\text{air}}}{l}$$

$$q \cdot 4\pi R^2 \approx \rho_a \cdot \frac{4}{3}\pi R^3 \cdot 3k \cdot K$$

$$K \approx \frac{\chi}{\rho_a \cdot R \cdot k} \frac{T - T_{\text{air}}}{l} \quad (2)$$

where $\chi = 0.027 \text{ W m}^{-1} \text{ K}^{-1}$ is the parameter for air thermal conductivity, $\rho_a = 4.9 \times 10^{30} \text{ m}^{-3}$ is the atomic silicon density, R is the nanoparticle radius, l is the thermal gradient length in the air stream, and T and T_{air} are the temperatures of the nanoparticle and air, respectively. These equations are given taking into account that the atomic heat capacity is equal to $3k$, where k is the Boltzmann constant. For $l = 100 \text{ nm}$ (double the value of the mean free path of the air molecules) and $T - T_{\text{air}} \approx 1000 \text{ K}$, we estimate that $K \approx K_0 \cdot (50/R)$, where $K_0 = 0.008 \text{ K ps}^{-1}$ and R is the radius in nanometers. These estimates are very rough and give the averaged values. For instance, the estimated cooling rate of the ablated nanoparticle with $T = 2000 \text{ K}$ is about $K_0 \cdot (85/R)$. However, the K is smaller by two orders of magnitude compared to the calculated K_{th} even taking into account the inaccuracies of the equations.

The performed analysis shows that the crystallization takes place in the moving nanoparticle, if it is strongly undercooled. Our previous calculations³⁸ show that crystallization begins at $T \approx 0.75T_m \approx 1250 \text{ K}$. For the estimation of a supercooling value, we use the model of a particle moving in viscous media. In this case, the equation for particle velocity v is:

$$\rho \frac{4}{3}\pi R^3 \frac{dv}{dt} = 6\pi\eta R \cdot v \quad (3)$$

where $\rho = 2300 \text{ kg m}^{-3}$ is the silicon mass density and $\eta = 1.9 \times 10^{-5} \text{ Pa s}$ is the viscosity coefficient. For the solution of eqn (3), velocity depends on time t as $v = v_0 \exp(-t/\tau)$, where v_0 is the initial particle velocity (about 100 m s^{-1}) and $\tau = 2\rho R^2 / 9\eta$ is the relaxation time. For this model, T of the nanoparticle that moved on distance z may be estimated as:

$$T \approx T_0 - K \cdot \tau \ln \frac{v_0 \tau}{v_0 \tau - z} \quad (4)$$

Eqn (4) allows us to roughly estimate the possibility of crystallization. Fig. 5 shows the estimation of laser printing para-

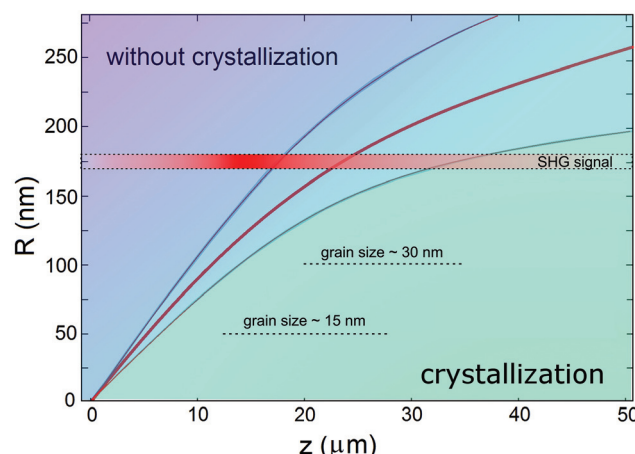


Fig. 5 Crystallization of liquid Si nanoparticles in air. The diagram of the Si nanoparticle crystalline state just before the moment of contact with the receiving substrate calculated from formulas (2)–(4). The green region (large values of z and small values of R) corresponds to nanoparticle crystallization by moving between substrates. The blue region (small values of z and large values of R) corresponds to the remainder of the nanoparticle in the liquid state during the flight in air, implying further crystallization on a substrate. The intermediate zone (containing the brown curve and two additional blue curves in the center) illustrates the uncertainty area, where the boundary between the regions is changed due to parameter variations in eqn (2) and (3): the initial temperature is varied in the range $T_0 = 1900\text{--}2100 \text{ K}$, the characteristic cooling rate $K_0 = 0.004\text{--}0.01 \text{ K ps}^{-1}$, and the initial speed of the nanoparticle $v_0 = 80\text{--}120 \text{ m s}^{-1}$. Horizontal dashed lines in the green region correspond to the average grain sizes in the crystallized nanoparticles. The red semi-transparent stripe schematically shows the experimentally observed SHG signal from $R = 175 \text{ nm}$ nanoparticles, where the intensity of the red color correlates with SHG intensity.

meters (R and z) that correspond to particle crystallization (the temperature decreases down to 1250 K). The uncertainty area of Fig. 5 illustrates the variation in the results at changes of the poorly defined parameters: K_0 from 0.004 K ps^{-1} to 0.01 K ps^{-1} ; T_0 from 1900 K to 2100 K ; and v_0 from 80 m s^{-1} to 120 m s^{-1} . Also, the estimates of average grain sizes in the nanoparticles are shown in the Fig. 5. The performed analysis shows that the crystallization of the printed nanoparticles in air takes place when distance $z > 15 \mu\text{m}$. This fact agrees well with the experimental data.

3.4. Cooling on a substrate

As shown in the previous section and in Fig. 5, the final stage of cooling and solidification of the Si nanoparticles ($z < 10 \mu\text{m}$ at $R \approx 175 \text{ nm}$) can occur on a substrate, but not in air. Under such conditions, the material properties of the substrate play a decisive role. For example, the glass thermal conductivity χ_g is approximately 40 times greater than the air one. However, the area of contact with the receiver surface is several times smaller than R^2 (it depends on particle state and wetting properties). In this case, the value of K can be about $0.3\text{--}0.5 \text{ K ps}^{-1}$. This cooling rate is close to the threshold value $K_{\text{th}} \approx 0.8 \text{ K ps}^{-1}$ determined in previous sections, and the amor-

phous-nanocrystal structure with an average grain size of about 7–8 nm mostly occurs. In addition, impurities, like hydrogen, facilitate the formation of such pseudo-amorphous structures. The strongest effect in SHG increasing takes place in the range of z from 10 μm to 20 μm that probably corresponds to the intermediate case: the crystallization is initiated in air just before contact with the substrate. In this case, rapid cooling of nanoparticles on the substrate suppresses such relaxation processes as recrystallization. It can be assumed that the nanocrystal structure with an average grain size of about 30–50 nm corresponds to the case when SHG is the most optimal.

Our model is also valid for the case of laser printing of silicon nanoparticles on a gold surface, *i.e.* the case of extremely fast cooling processes owing to the two orders of magnitude higher thermal conductivity of gold than that of glass. As shown in ESI,[†] at short distances ($z = 10 \mu\text{m}$) the printed silicon particles are splashed and frozen before the surface tension makes them spherical.

4. Conclusion

To summarize, we have proposed and studied a novel technique to control the crystalline structure of silicon nanoparticles fabricated by laser printing from the almost amorphous to the polycrystalline state. In particular, we have applied the method of crystalline structure control *via* changing the distance between the irradiated silicon film and the receiver substrates. We have observed the maximum second harmonic yield at distances in the range of 10–20 μm corresponding to some presence of the amorphous phase and a grain size of around 40 nm.

Our results shed light on the origin of different crystalline phases of the printed silicon nanoparticles at different distances observed in various experiments.^{9,11,13,15} Also, these results help to control crystallization processes in other advanced heating-based methods for silicon nanostructure fabrication.^{39–42} We believe that the proposed method paves the way for fully controllable fabrication of functional nanoparticles and nanostructures by using high-throughput methods.

Conflicts of interest

There are no conflicts to declare.

Acknowledgements

S. M. is thankful to the Ministry of Education and Science of the Russian Federation (Project 14.Y26.31.0010 for supporting the optical measurements). L. K. and S. V. S. are thankful to the Russian Foundation for Basic Research (grants 17-03-00621 for supporting the theoretical analysis). U. Z. and B. C. acknowledge financial support from the DFG grants

(CH 179/34-1 and RE 3012/4-1), and the Grant of Russian Science Foundation No. 16-13-10528 for supporting nanoparticle generation experiments.

References

- 1 A. Kuznetsov, R. Kiyan and B. Chichkov, *Opt. Express*, 2010, **18**, 21198–21203.
- 2 A. I. Kuznetsov, A. B. Evlyukhin, M. R. Goncalves, C. Reinhardt, A. Koroleva, M. L. Arnedillo, R. Kiyan, O. Marti and B. N. Chichkov, *ACS Nano*, 2011, **5**, 4843–4849.
- 3 C. W. Visser, R. Pohl, C. Sun, G.-W. Römer, B. Huis int Veld and D. Lohse, *Adv. Mater.*, 2015, **27**, 4087–4092.
- 4 A. B. Evlyukhin, S. M. Novikov, U. Zywietsz, R. L. Eriksen, C. Reinhardt, S. I. Bozhevolnyi and B. N. Chichkov, *Nano Lett.*, 2012, **12**, 3749–3755.
- 5 Y. H. Fu, A. I. Kuznetsov, A. E. Miroshnichenko, Y. F. Yu and B. Lukyanchuk, *Nat. Commun.*, 2013, **4**, 2538.
- 6 J. Yan, P. Liu, Z. Lin, H. Wang, H. Chen, C. Wang and G. Yang, *ACS Nano*, 2015, **9**, 2968–2980.
- 7 J. Yan, C. Ma, P. Liu, C. Wang and G. Yang, *Nano Lett.*, 2017, **17**, 4793–4800.
- 8 J. Yan, P. Liu, Z. Lin and G. Yang, *Nanoscale*, 2016, **8**, 5996–6007.
- 9 S. V. Makarov, M. I. Petrov, U. Zywietsz, V. Milichko, D. Zuev, N. Lopanitsyna, A. Kuksin, I. Mukhin, G. Zografi, E. Ubyivovk, *et al.*, *Nano Lett.*, 2017, **17**, 3047–3053.
- 10 G. P. Zografi, M. I. Petrov, D. A. Zuev, P. A. Dmitriev, V. A. Milichko, S. V. Makarov and P. A. Belov, *Nano Lett.*, 2017, **17**, 2945–2952.
- 11 V. Milichko, D. Zuev, D. Baranov, G. Zografi, K. Volodina, A. Krasilin, I. Mukhin, P. Dmitriev, V. Vinogradov, S. Makarov and P. A. Belov, *Laser Photonics Rev.*, 2018, **12**, 1700227.
- 12 M. L. De Marco, S. Semlali, B. A. Korgel, P. Barois, G. L. Drisko and C. Aymonier, *Angew. Chem.*, 2018, **57**(17), 4478–4498.
- 13 U. Zywietsz, A. B. Evlyukhin, C. Reinhardt and B. N. Chichkov, *Nat. Commun.*, 2014, **5**, 3402.
- 14 U. Zywietsz, M. K. Schmidt, A. B. Evlyukhin, C. Reinhardt, J. Aizpurua and B. N. Chichkov, *ACS Photonics*, 2015, **2**, 913–920.
- 15 P. A. Dmitriev, D. G. Baranov, V. A. Milichko, S. V. Makarov, I. S. Mukhin, A. K. Samusev, A. E. Krasnok, P. A. Belov and Y. S. Kivshar, *Nanoscale*, 2016, **8**, 9721–9726.
- 16 U. Zywietsz, T. Fischer, A. Evlyukhin, C. Reinhardt and B. Chichkov, *Laser Printing of Functional Materials: 3D Microfabrication, Electronics and Biomedicine*, 2018.
- 17 D. Zhigunov, A. B. Evlyukhin, A. S. Shalin, U. Zywietsz and B. N. Chichkov, *ACS Photonics*, 2018, **5**(3), 977–983.
- 18 P. A. Dmitriev, S. V. Makarov, V. A. Milichko, I. S. Mukhin, A. S. Gudovskikh, A. A. Sitnikova, A. K. Samusev, A. E. Krasnok and P. A. Belov, *Nanoscale*, 2016, **8**, 5043–5048.

- 19 Z. Iqbal and S. Veprek, *J. Phys. C: Solid State Phys.*, 1982, **15**, 377.
- 20 S. V. Makarov, I. S. Sinev, V. A. Milichko, F. E. Komissarenko, D. A. Zuev, E. V. Ushakova, I. Mukhin, Y. Yu, A. I. Kuznetsov, P. A. Belov, *et al.*, *Nano Lett.*, 2018, **18**, 535–539.
- 21 J. Perez, J. Villalobos, P. McNeill, J. Prasad, R. Cheek, J. Kelber, J. Estrera, P. Stevens and R. Glosser, *Appl. Phys. Lett.*, 1992, **61**, 563–565.
- 22 P. Guyot-Sionnest, W. Chen and Y. Shen, *Phys. Rev. B: Condens. Matter Mater. Phys.*, 1986, **33**, 8254.
- 23 P. Guyot-Sionnest and Y. Shen, *Phys. Rev. B: Condens. Matter Mater. Phys.*, 1988, **38**, 7985.
- 24 W. L. Mochán, J. A. Maytorena, B. S. Mendoza and V. L. Brudny, *Phys. Rev. B: Condens. Matter Mater. Phys.*, 2003, **68**, 085318.
- 25 P. Ginzburg, A. V. Krasavin, G. A. Wurtz and A. V. Zayats, *ACS Photonics*, 2014, **2**, 8–13.
- 26 P. R. Wiecha, A. Arbouet, H. Kallel, P. Periwal, T. Baron and V. Paillard, *Phys. Rev. B: Condens. Matter Mater. Phys.*, 2015, **91**, 121416.
- 27 P. R. Wiecha, A. Arbouet, C. Girard, T. Baron and V. Paillard, *Phys. Rev. B*, 2016, **93**, 125421.
- 28 S. V. Starikov and V. V. Pisarev, *J. Appl. Phys.*, 2015, **117**, 135901.
- 29 S. I. Anisimov, V. Zhakhovsky, N. Inogamov, S. A. Murzov and V. A. Khokhlov, *Quantum Electron.*, 2017, **47**, 509.
- 30 A. I. Kuznetsov, C. Unger, J. Koch and B. N. Chichkov, *Appl. Phys. A*, 2012, **106**, 479–487.
- 31 C. Unger, J. Koch, L. Overmeyer and B. N. Chichkov, *Opt. Express*, 2012, **20**, 24864–24872.
- 32 T. C. Röder and J. R. Köhler, *Appl. Phys. Lett.*, 2012, **100**, 071603.
- 33 M. D. Kluge, J. R. Ray and A. Rahman, *J. Chem. Phys.*, 1987, **87**, 2336–2339.
- 34 S. Link, C. Burda, M. Mohamed, B. Nikoobakht and M. A. El-Sayed, *J. Phys. Chem. A*, 1999, **103**, 1165–1170.
- 35 R. Pohl, C. W. Visser, G.-W. Römer, D. Lohse, C. Sun, B. Huis, *et al.*, *Phys. Rev. Appl.*, 2015, **3**, 024001.
- 36 D. Ivanov, A. Kuznetsov, V. Lipp, B. Rethfeld, B. Chichkov, M. Garcia and W. Schulz, *Appl. Phys. A*, 2013, **111**, 675–687.
- 37 N. Inogamov, V. Zhakhovskii and V. Khokhlov, *J. Exp. Theor. Phys.*, 2015, **120**, 15–48.
- 38 S. Starikov, N. Y. Lopanitsyna, D. Smirnova and S. Makarov, *Comput. Mater. Sci.*, 2018, **142**, 303–311.
- 39 M. Abbarchi, M. Naffouti, B. Vial, A. Benkouider, L. Lermusiaux, L. Favre, A. Ronda, S. Bidault, I. Berbezier and N. Bonod, *ACS Nano*, 2014, **8**, 11181–11190.
- 40 M. Naffouti, R. Backofen, M. Salvalaglio, T. Bottein, M. Lodari, A. Voigt, T. David, A. Benkouider, I. Fraj, L. Favre, *et al.*, *Sci. Adv.*, 2017, **3**, eaao1472.
- 41 B. Xiang, D. J. Hwang, J. B. In, S.-G. Ryu, J.-H. Yoo, O. Dubon, A. M. Minor and C. P. Grigoropoulos, *Nano Lett.*, 2012, **12**, 2524–2529.
- 42 J.-H. Yoo, J. B. In, C. Zheng, I. Sakellari, R. N. Raman, M. J. Matthews, S. Elhadj and C. P. Grigoropoulos, *Nanotechnology*, 2015, **26**, 165303.